Inorganic Chemistry

pubs.acs.org/IC

Article

Oxidation of Ethanol to Acetic Acid by Supported PtCu Nanoparticles Stabilized by a Diamine Ligand

Werner Oberhauser,* Lorenzo Poggini, Laura Capozzoli, Marco Bellini, Jonathan Filippi, and Francesco Vizza

Cite This: https://doi.org/10.1021/acs.inorgchem.2c04202

Read Online

ACCESS | Metrics & More | Article Recommendations | Supporting Information

ABSTRACT: Diamine-capped PtCu nanoparticles have been synthesized by the simultaneous reduction of the corresponding bis-imine metal complexes with hydrogen and supported onto a high-surface-area carbon. The obtained heterogeneous catalyst was tested in thermally conducted aerobic oxidation of ethanol to acetic acid in water as well as in the electrochemical oxidation of ethanol. Both types of catalyses mediated by the PtCu alloy confirmed a notable increase in catalytic activity compared to the pure Pt- and Cu-based counterparts due to a clear bimetallic effect.

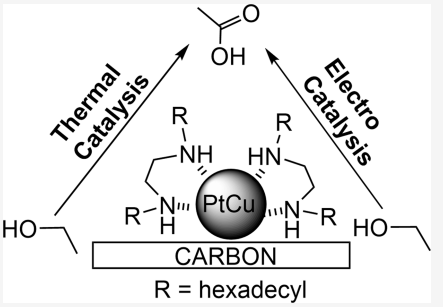

INTRODUCTION

Acetic acid (AA) is an important platform chemical, which finds major applications in the synthesis of vinyl acetate, acetic acid anhydride, and esters used as solvents for inks, paints, and coatings.[1] Furthermore, AA is also very important in the food sector, being a food additive and preservative with antimicrobial activity.[1] Food-grade AA is mainly obtained by the fermentative synthesis route, while the traditional chemical synthesis is based on the carbonylation of methanol by means of homogeneous Rh- and Ir-based catalysts[2] or by direct oxidation of ethylene with heterogeneous Pd-based catalysts at 423 K.[3] Both latter syntheses processes have shortcomings from a sustainability point of view. An alternative hence synthesis protocol for AA might consist of the selective transformation of biomass-originating substrates by means of robust heterogeneous catalysts, using water as the solvent and oxygen (air) as the final oxidant. In this context, ethanol (EtOH), obtained from fermentation of biomass, is an attractive substrate, while 1,2-propandiol (1,2-PD), gained by hydrogenolysis of glycerol,[4−7] yields stoichiometric amounts of CO_2 by its conversion to AA.[4]

The most efficient heterogeneous catalysts known for the aerobic EtOH-to-AA conversion are mainly Au-[5−8] and Ru-based.[9,10] Heterogeneous Pt-based catalysts have the advantage of being active in the absence of an extra base, thus avoiding the generation of huge amounts of inorganic salt. To reduce the amount of platinum used for the catalytic process, alloy NPs formed between Pt and other non-noble metals are important. In particular, PtCu alloy NPs, which have been mostly employed as electrocatalysts for alcohol and polyol oxidation reactions,[11−15] for the aerobic oxidation of benzyl alcohol,[16,17] as a catalyst for thermal NO_x reduction[18] and glycerol hydrogenolysis to 1,2-PD,[19] are very promising since the synergistic effect between both metals (*i.e.*, Cu electron donor and Pt electron acceptor) might increase the catalytic activity compared to the pure Pt counterpart. A major hurdle in the synthesis of well-defined PtCu NPs is the fact that the composition of Pt_xCu_{1-x} alloy NPs[20,21] can vary notably (*i.e.*, $0 \leq x \leq 1$) and the final alloy composition depends not only on the metal ratio used but also on the reaction conditions (*i.e.*, reaction temperature, precursor, and capping ligand used).[22,23]

Herein, we show that the synthesis of diamine-stabilized PtCu NPs, characterized by a Pt-to-Cu atom ratio of 1 by the simultaneous reduction of a Pt(II) and Cu(II)-bis-imine complex, is a suitable synthesis procedure. A secondary diamine ligand with hexadecyl chains and an ethylene spacer in between the nitrogen atoms was chosen as the stabilizing ligand for the PtCu and its Pt and Cu counterparts for the following reasons: (i) NPs are stabilized by the steric effect exerted by the long aliphatic chains; (ii) stronger coordination to the surface metal atoms of the NPs by exploiting the chelating effect compared; (iii) nitrogen functionalities are stable under aerobic oxidation reaction conditions; (iv) the ligand is completely insoluble in polar solvents such as water and low-molecular-weight alcohols, thus avoiding leaching of the ligand from heterogeneous support; and (v) the secondary amine functionalities might be exploited as proton or

Received: November 28, 2022

Scheme 1. Syntheses of $Pt^L/(PtCu)^L/Cu^L@C^K$

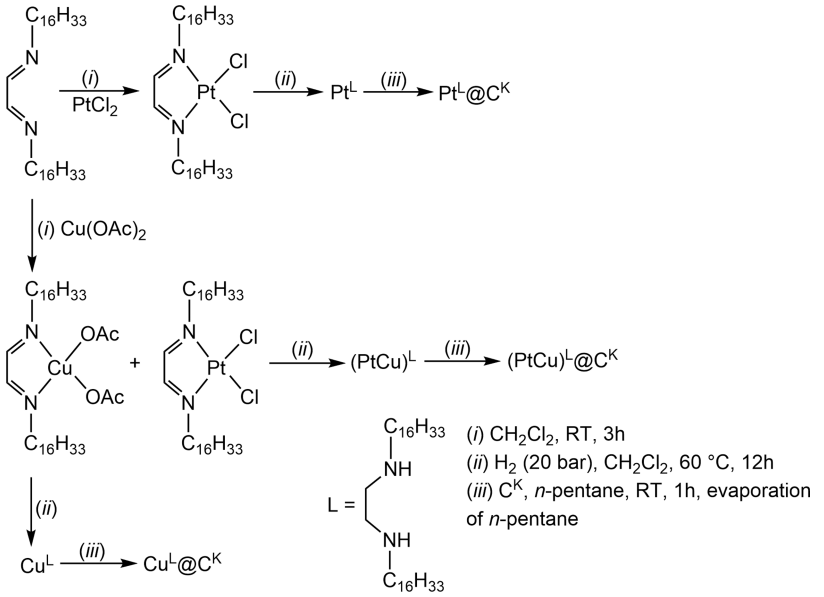

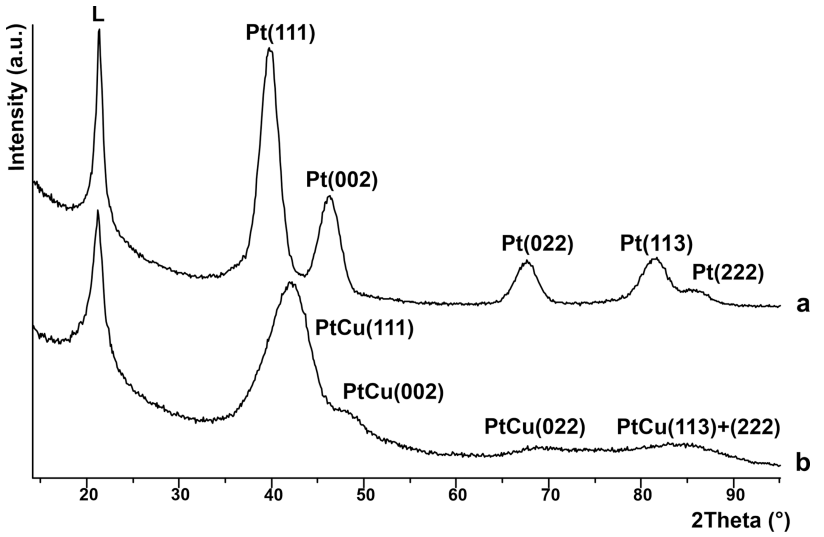

Figure 1. PXRD spectra of as-synthesized Pt^L (a) and $(PtCu)^L$ (b).

hydroxide shuttle in close proximity to the catalytically active surface metal atoms, which is important in aerobic and electrochemically conducted oxidation reactions. The carbon-supported capped-bimetallic NPs were screened for EtOH oxidation under thermal and aerobic as well as under electrochemical conditions to yield AA.

RESULTS AND DISCUSSION

Synthesis and Characterization of Catalysts. The diamine (L)-capped PtCu NPs and their Pt and Cu counterparts (*i.e.*, $(PtCu)^L$, Pt^L, and Cu^L) have been obtained following a synthesis protocol, which comprises two important reaction steps (Scheme 1): (i) the coordination of the metal(II) salts to *N*,*N*′-bis-(*n*-hexadecyl)α-diimine in dichloromethane at room temperature; and (ii) the reduction of the coordination compound with hydrogen gas (20 bar) in dichloromethane at 333 K for 12 h in an autoclave. In the case of $(PtCu)^L@C^K$, a 1:1 mixture of Pt(II) and Cu(II) bis-imine coordination compounds was dissolved in dichloromethane and used for synthesis step ii (Scheme 1) During the reduction step with hydrogen (step ii), a suspension was obtained, which consisted of L-stabilized NPs (soluble in dichloromethane) and the ammonium salt of the ligand, which is only partially soluble in dichloromethane. The ammonium salt was then separated from the L-stabilized NPs by evaporation of the dichloromethane suspension, addition of *n*-pentane, and filtration of the suspension. The *n*-pentane solution was concentrated to dryness, and the solid was analyzed by ICP-OES prior to dissolving it again, mixing with a sonicated suspension of carbon (Ketjenblack EC-600 JD, C^K) followed by the evaporation of the solvent (Scheme 1, step iii).

The isolated powders of $(PtCu)^L$, Pt^L, and Cu^L have been analyzed by ICP-OES, showing for $(PtCu)^L$ Pt and Cu contents of 13.94 and 4.86 wt %, respectively; for Pt^L, a Pt content of 15.81 wt %; and for Cu^L, a Cu content of only 1.88 wt %, which is in agreement with the observation that during the workup of Cu^L, we observed the presence of a precipitate, which corresponded, according to PXRD analysis, to

https://doi.org/10.1021/acs.inorgchem.2c04202
Inorg. Chem. XXXX, XXX, XXX−XXX

unstabilized Cu NPs (Figure S1). This experimental result indicates that the lower reduction potential of Cu(II)/Cu(0) compared to Pt(II)/Pt(0) (0.34 *vs* 1.2 V) avoided the formation of many nucleation events, and as a consequence, these latter seeds grew slowly, resulting in larger NPs compared to those obtained in the case of Pt^L.[24] The coordinating ligand seems not to have a fundamental role in controlling the end size of the Cu NPs, which has been corroborated by a significantly larger standard deviation observed for Cu^L NPs compared to the Pt counterparts.

The PXRD spectrum acquired at room temperature for Pt^L (Figure 1, trace a) clearly exhibited the Bragg reflexes characteristic for the *fcc*-Pt metal phase, with the most intense Pt (111) reflex centered at 39.73° (2Θ). The analogous PXRD spectrum for $(PtCu)^L$ (Figure 1, trace b) showed that the PtCu (111) Bragg reflex centered at 42.01 ° (2Θ) shifted to a higher 2Θ compared to Pt^L due to the smaller elementary cell present in PtCu compared to Pt.[11,13] Importantly, both PXRD spectra show a narrow Bragg reflex at 21.32° (2Θ), which has been assigned to the crystalline part of the capping ligand. The average NPs' sizes for Pt^L and $(PtCu)^L$, determined by the Debye−Scherrer method[25] and based on the corresponding (111) reflexes, were shown to be 3.7 and 2.2 nm, respectively.

XPS analysis conducted on $(PtCu)^L$ (Figure 2a, Table S1) showed for surface Pt atoms the occurrence of three oxidation states: B.E. of Pt $4f_{7/2}$ 70.4 eV, Pt(0); 72.5 eV, Pt(II); and 74.5 eV, Pt(IV), with Pt(0) (56.2%) being the most abundant one.[26] Pt^L showed the same surface Pt oxidation states as $(PtCu)^L$, which slightly (0.1 eV) shifted to higher B.E. (*i.e.*, B.E. of Pt $4f_{7/2}$ 70.5 eV, Pt(0); 72.6 eV, Pt(II); and 74.6 eV, Pt(IV)). The Pt(II) oxidation state is much more present in $(PtCu)^L$ (39.2%) than in Pt^L (14.1%), indicating a much more easier oxidation of Pt(0) in the presence of Cu (*i.e.*, electron-donating effect of Cu), which is also in agreement with the slightly lower B.E.s found for the Pt(0-IV) oxidation states in the case of $(PtCu)^L$ compared to Pt^L.

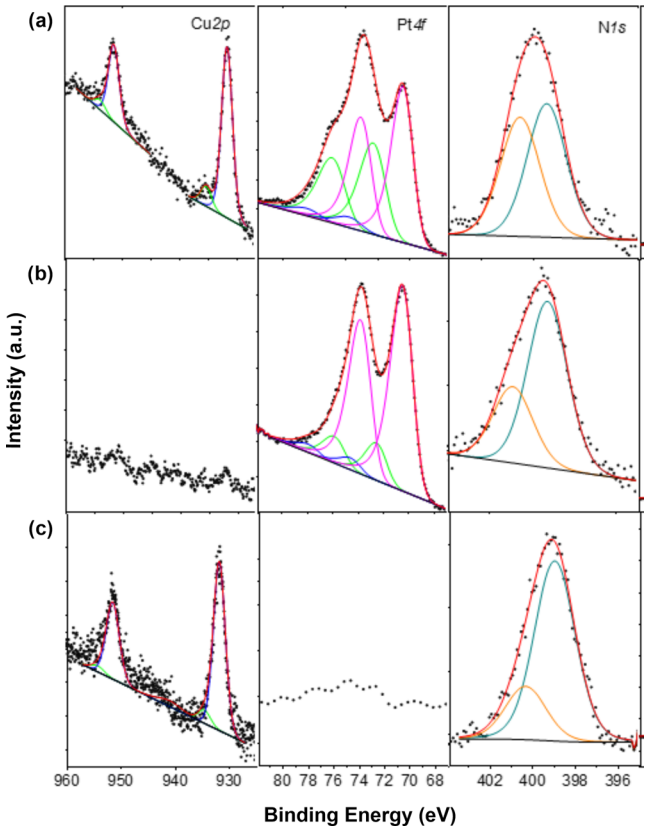

Figure 2. XPS spectra in the Cu2p, Pt4f, and N1s regions for $(PtCu)^L$ (a), Pt^L (b), and Cu^L (c).

The Cu $2p_{3/2}$ photoelectron spectrum for $(PtCu)^L$ exhibited two contributions at B.E. 931.6 and 935.2 eV, which have been assigned to Cu(0) and Cu(II) surface species, respectively.[27,28] The surface Pt-to-Cu atom ratio in $(PtCu)^L$ was found to be 0.5, indicating an excess of Cu atoms with respect to Pt on the NPs' surface, which is in accordance with a more difficult reduction of Cu(II) compared to Pt(II). The bulk analysis $(PtCu)^L$ carried out by ICP-OES gave a Pt and Cu molar ratio of 0.93, which is close to 1, expected for a 1:1 PtCu alloy.

The N *1s* photoelectron peak for the diamine ligand in Pt^L and $(PtCu)^L$ has been deconvoluted in two components centered at B.E. 399.3 and 400.6 eV (Table S1). The former B.E. is shifted to a higher B.E. (1.1. eV) compared to uncoordinated L (B.E. 398.2 eV) (Figure S2), confirming hence the interaction of the amine nitrogen atoms of L with the NPs' surface atoms, whereas the B.E. of 400.6 eV was assigned to hydrogen-bond interactions between the capping amine functionalities and surface metal hydroxide species.[29,30] A comparison of the N *1s* B.E. for Pt^L, $(PtCu)^L$, and Cu^L gave an indication that the amine nitrogen atoms of L interact with surface Pt(0) atoms of $(PtCu)^L$.

The interaction of the capping ligand with the NP surface of Pt^L and $(PtCu)^L$ has been further studied by ^1H NMR spectroscopy. To this purpose, spectra have been acquired in C_6H_6-d_6 for L, Pt^L, and $(PtCu)^L$ (Figure 3). Upon coordination of L to the NP surface atoms, the singlet centered at 2.78 ppm (i.e., N-CH_2CH_2-N) and the triplet at 2.69 ppm ($^3J_{HH}$ = 7.4 Hz, CH_2-R), both signals assigned to the uncoordinated L (Figure 3, trace a), experienced a shift to a lower frequency in Pt^L (i.e., 2.62 ppm and 2.42 ppm, respectively) (Figure 3, trace b), which is in accordance with a shielding of these protons. In addition, the chemical shifts observed for the above-mentioned hydrogen atoms in $(PtCu)^L$ were comparable to that of Pt^L, and thus, we concluded that L coordinates to surface Pt(0) atoms of $(PtCu)^L$.

The C^K-supported catalysts $Pt^L@C^K$ and $(PtCu)^L@C^K$ have been analyzed by TEM, PXRD, and BET measurements. As a result, TEM images and the corresponding histograms for $Pt^L/(PtCu)^L@C^K$ (Figure 4) showed the presence of small, spherically shaped NPs with a narrow size distribution (*i.e.*, $Pt^L@C^K$, d_m = 3.43 ± 0.43 nm and $(PtCu)^L@C^K$, d_m = 2.18 ± 0.23 nm). The latter NP sizes matched well with those of the unsupported catalysts (*i.e.*, Pt^L, 3.7 nm and $(PtCu)^L$, 2.2 nm). Unlike Pt^L and $(PtCu)^L$, Cu^L showed the largest NP size and size distribution (*i.e.*, d_m = 4.35 ± 0.89, Figure S3)

PXRD spectra acquired for $Pt^L@C^K$ (Pt loading of 0.75 wt %) and $(PtCu)^L@C^K$ (Pt loading of 0.34 wt %) (Figure 5, traces b and c, respectively) showed only in the former case a Bragg reflex assigned to the metal phase (*i.e.*, Pt (111) at 39.73 (2Θ)) due to the higher Pt loading and larger NP size in $Pt^L@C^K$ compared to $(PtCu)^L@C^K$. On the other hand, the PXRD spectrum of $(PtCu)^{L'}@C^K$ (Figure 5, trace d), featured by a Pt loading of 2.04 wt %, showed an asymmetric peak at ca. 43.0° (2Θ), which deconvoluted in two broad Bragg peaks (*i.e.*, PtCu (111) at 42.0° (2Θ) and a broad peak stemming from C^K (Figure 5, trace a)). In addition, the PXRD spectrum of $(PtCu)^{L'}@C^K$ showed for the capping ligand a broad

https://doi.org/10.1021/acs.inorgchem.2c04202
Inorg. Chem. XXXX, XXX, XXX−XXX

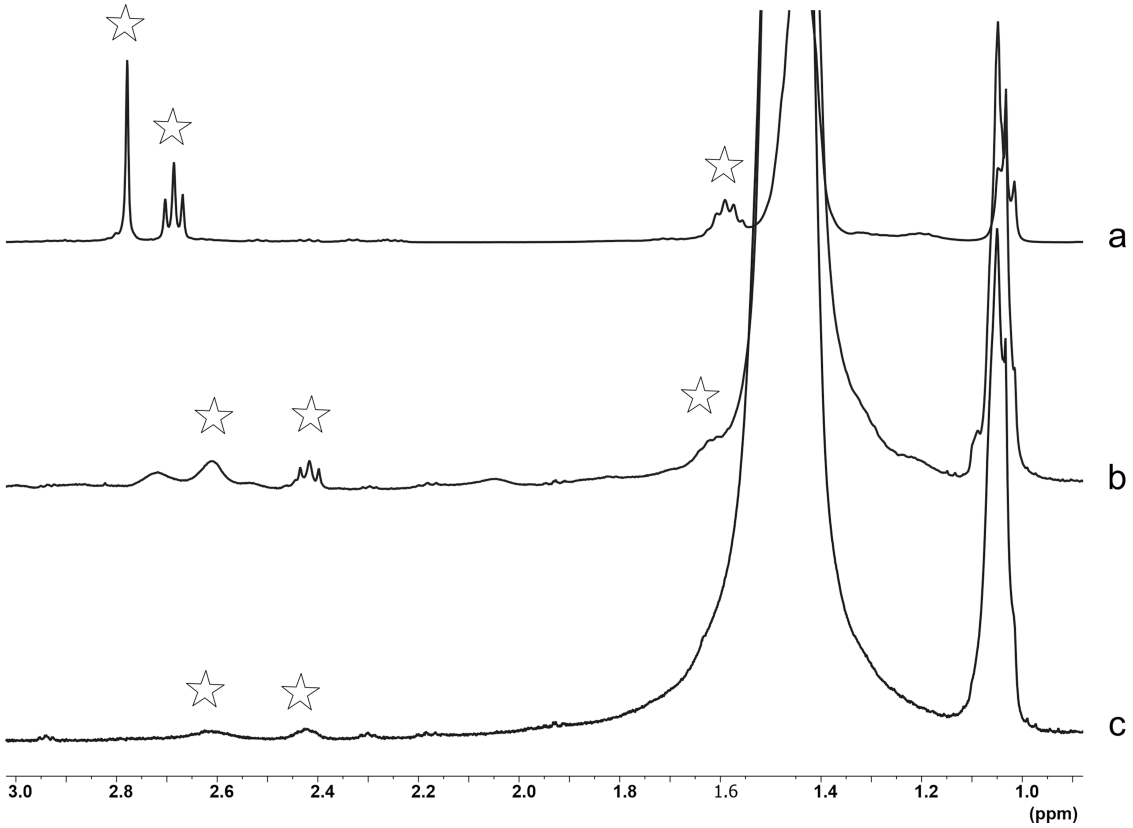

Figure 3. ^{1}H NMR spectra acquired in C_6H_6-d_6 for L (a), Pt^{L} (b), and $(PtCu)^{L}$ (c). Asterisks denote the relevant ^{1}H NMR signals involved in the interaction of L with the NP surface atoms.

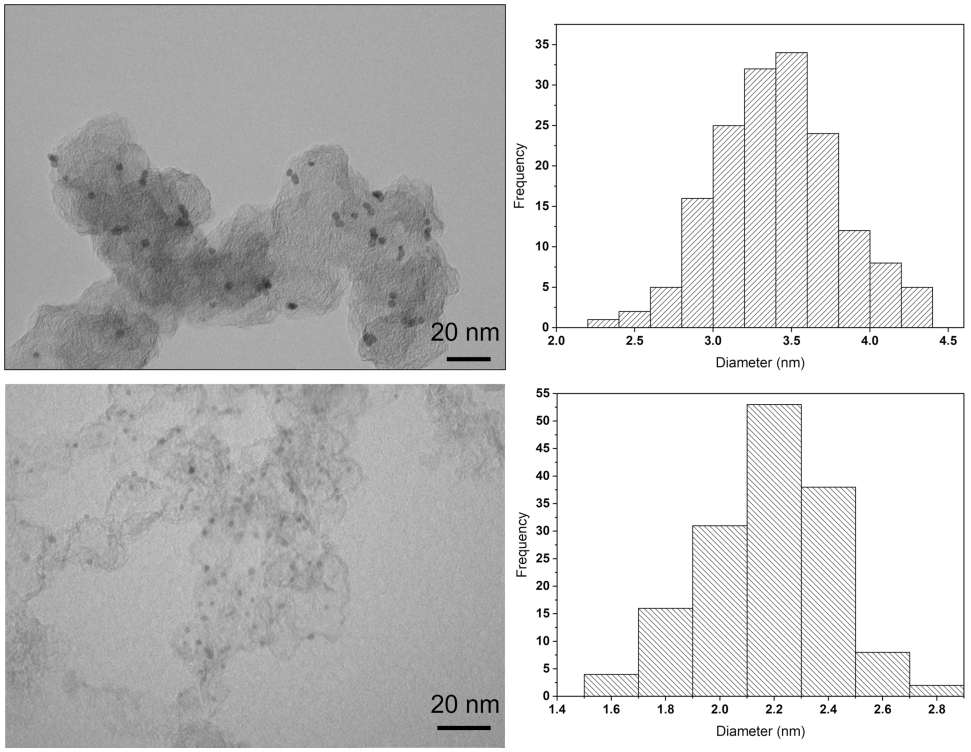

Figure 4. TEM micrographs and histograms for $Pt^{L}@C^{K}$ (upper, d_m = 3.43 ± 0.43 nm) and $(PtCu)^{L}@C^{K}$ (lower, d_m = 2.18 ± 0.23 nm).

diffraction hump between 19 and 25° (2Θ), which is indicative of an amorphous phase for L, due to the NP dispersion and ligand interaction with the support surface.[31]

BET analyses conducted for $Pt^{L}@C^{K}$ (Figure S4) and $PtCu^{L}@C^{K}$ (Figure S5 and Table S2) were based on nitrogen physisorption and revealed for both catalysts a similar but

https://doi.org/10.1021/acs.inorgchem.2c04202
Inorg. Chem. XXXX, XXX, XXX−XXX

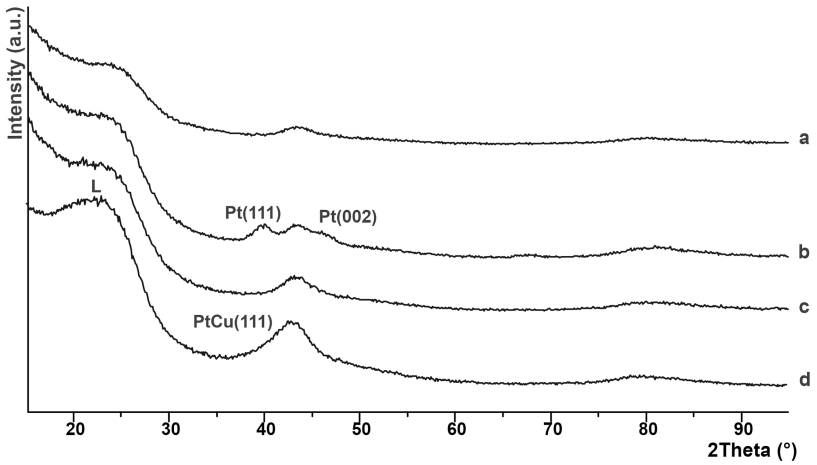

Figure 5. PXRD spectra acquired at room temperature for C^K (a), $Pt^L@C^K$ (b), $(PtCu)^L@C^K$ (c), and $(PtCu)^{L'}@C^K$ (d).

Table 1. Catalytic Aerobic Oxidation of EtOH and AcA in Water[a,b,c,d,e,f,g,h,i]

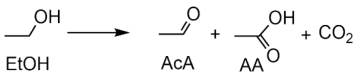

Entry	Catalyst/Pt (μmol)	Conv. (%)[b]/[TON][c]	Sel. AcA (%)[d]	Sel.[d]/Yield[e] AA (%)	CO_2 (%)[f]
1	-	14.6	84.5	15.5/2.2	-
2	$Pt^L@C^K$ (1.92)	50.4/[3596]	64.3	35.7/10.9	19.8
3[g]	$Pt^L@C^K$ (1.92)	92.5/[6600]	14.4	85.6/47.4	37.1
4	$(PtCu)^L@C^K$ (0.94)	40.9/[5961]	70.3	29.7/59.1	15.1
5[g]	$(PtCu)^L@C^K$ (0.94)	97.5/[14210]	1.4	98.6/73.3	23.2
6	$(PtCu)^{L'}@C^K$ (5.23)	44.2/[1158]	62.6	37.4/12.4	11.0
7[h]	$Cu^L@C^K$	22.6/n.d.	66.0	34.0/4.3	10.0

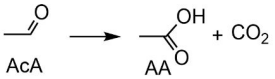

8[i]	-	98.2	-	-/89.8	8.5
9[i]	$Pt^L@C^K$ (1.92)	98.7/[7043]	-	-/70.8	27.9
10[i]	$(PtCu)^L@C^K$ (0.94)	97.1/[14152]	-	-/83.7	13.4
11[h,i]	$Cu^L@C^K$	90.1/n.d.		-/70.8	19.3

[a]Catalytic condition: EtOH (13.7 mmol), water (50.0 mL), p(air) = 20 bar at 413 K, t (17 h), T (413 K). [b]Conv. (%) defined as: 100 × [mmol (substrate initial) − mmol (substrate recovered)]/mmol (substrate initial). [c]TON defined as: mmol (substrate converted)/mmol (Pt). [d]Sel. (%) defined as: 100 × [mmol (product)/∑ mmol (AcA + AA)]. [e]Yield (%) defined as: 100 × [mmol (AA)/mmol (substrate initial)]. [f]CO_2 (%) defined as: 100 × [mmol (substrate initial) − mmol (substrate recovered) − ∑ mmol (products)] / mmol (substrate initial). [g]t (40 h). [h]Cu (4.40 μmol). [i]AcA (13.7 mmol), t(3 h).

slightly lower surface area compared to C^K (*i.e.*, $Pt^L@C^K$, 1352.6 m^2/g; $(PtCu)^L@C^K$, 1267.7 m^2/g; and C^K, 1500 m^2/g[30]). By increasing the loading of $(PtCu)^L$ on C^K, as in the case of $(PtCu)^{L'}@C^K$, the BET surface area dropped significantly (846.37 m^2/g) (Figure S6). Due to the higher metal loading in $(PtCu)^{L'}@C^K$ compared to $(PtCu)^L@C^K$, we were able to carry out a reliable XPS analysis with the former supported catalyst. The related XPS data have been compiled in Table S1 and are in line with those found for $(PtCu)^L$, which proves that the capped NPs did not undergo alteration during their heterogenization on C^K.

Catalytic Aerobic Oxidation of EtOH in Water. $Pt^L/(PtCu)^L/Cu^L@C^K$ has been screened for the aerobic oxidation of EtOH in water, applying identical experimental conditions (*i.e.*, EtOH (0.27 M), T (413 K), p(air) (20 bar), t (17 h)). To avoid mass-transfer limitations during the catalytic reactions, the stirring speed of the magnetically mixed suspensions was optimized (900 rpm). The catalytic solutions have been analyzed by HPLC (Figure S7) and ^1H NMR spectroscopy (Figure S8) after the solid catalysts had been separated from solution. The results of the catalytic reactions have been compiled in Table 1. The aerobic oxidation of EtOH applying the above-mentioned experimental conditions and in the absence of a metal catalyst gave a conversion of 14.6% with acetaldehyde (AcA) as the major reaction product (Table 1, entry 1), whereas in the presence of the heterogeneous catalysts, the EtOH conversion and AA selectivity notably increased (Table 1). The observed catalytic activity increased in the order $Cu^L@C^K < Pt^L@C^K < (PtCu)^L@C^K$ (Table 1). In addition, at high EtOH conversion (>90%), the much higher catalytic activity, AA selectivity, and yield obtained with the bimetallic catalyst compared to the pure Pt-based catalyst are evident (Table 1, entry 5 *vs* 3). Interestingly, $(PtCu)^{L'}@C^K$, which is featured by a higher loading of bimetallic NPs compared to $(PtCu)^L@C^K$, gave a notably lower TON compared to the diluted case (Table 1, entry 6 *vs* 4). This

https://doi.org/10.1021/acs.inorgchem.2c04202
Inorg. Chem. XXXX, XXX, XXX−XXX

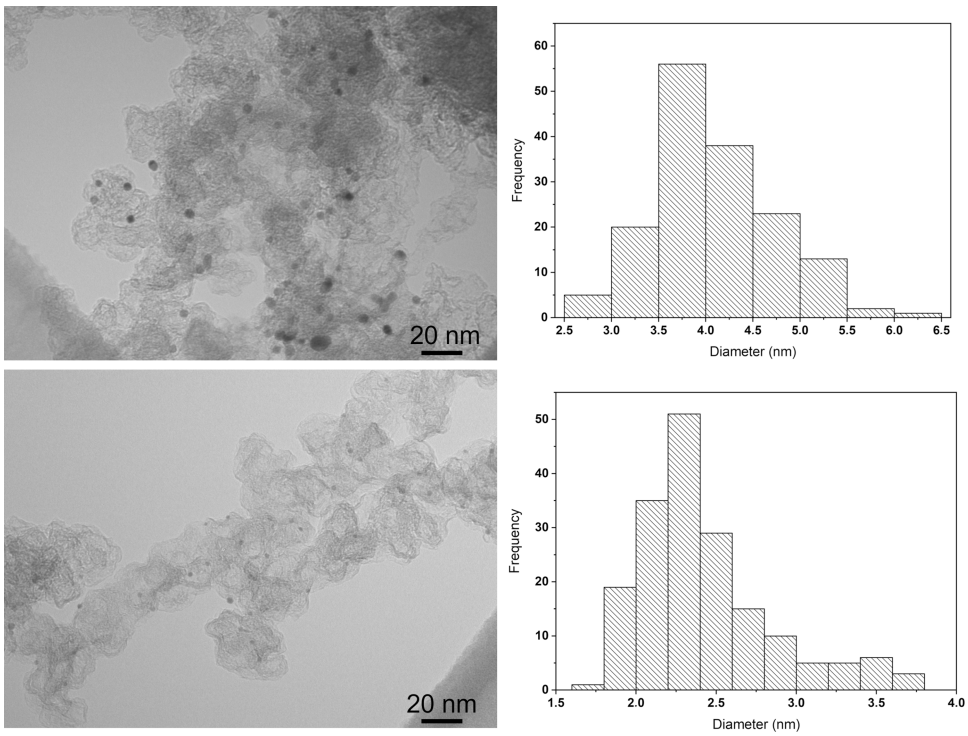

Figure 6. TEM micrographs and histograms for the recovered $Pt^{L}@C^{K}$ (upper, d_m = 4.08 ± 0.65 nm) and $(PtCu)^{L}@C^{K}$ (lower, d_m = 2.44 ± 0.43 nm).

experimental result strongly indicates that upon increasing the loading of the PtCu NPs on C^{K}, the sterically demanding capping ligand covers to a certain extent the NPs disfavoring the substrate access to the catalytically active reaction sites located on the NPs' surface, bringing about a drop of the catalytic activity. The headspace analysis (GC-TCD, Figure S9) of the autoclave conducted after catalysis confirmed the formation of CO_2 during the aerobic EtOH oxidation to AA (Table 1). The percentage of EtOH converted to CO_2 is the highest with $Pt^{L}@C^{K}$, while under comparable EtOH conversion, less CO_2 is formed when the bimetallic catalysts are used (*i.e.*, > 90.0% EtOH conversion, 37.1 *vs* 23.2% CO_2 formed). To better understand the origin of CO_2 formation during aerobic EtOH oxidation, we carried out analogous oxidation reactions using AcA as the substrate (Table 1, entries 8−11). At 413 K, the aerobic oxidation of AcA was fast, even in the absence of metal-based catalysts (*i.e.*, AcA is known to undergo radical-based conversion into AA in water and in the presence of oxygen),[32] and 8.5% CO_2 was formed at almost complete AcA conversion to AA (Table 1, entry 8). Analogous catalytic reactions in the presence of the NP-based catalysts gave at almost complete AcA conversion the highest AA yield and the lowest CO_2 formation for the bimetallic catalyst (Table 1, entry 10 *vs* 9 and 11). The higher amount of CO_2 formed during AcA oxidation in the presence of metal catalysts, compared to the uncatalyzed case, confirmed that CO_2 is formed during the activation of acetaldehyde by the metal catalyst, which is furthermore underscored by the experimental fact that AA is stable under the catalytic conditions given in Table 1, even in the presence of a metal-based catalyst (*i.e.*, 3% AA conversion to CO_2 after 17 h, T 413 K, *p*(air) 20 bar).

A comparison of the catalytic performance of $(PtCu)^{L}@C^{K}$ with other catalysts, known for the aerobic EtOH oxidation to AA, revealed that only a Ru(0) NP-based catalyst confined into layered double hydroxides (LDHs) gave similar catalytic results (*i.e.*, AA selectivity: 95.6% at an EtOH conversion of 94.1%, yield AA, 90.0%) using a higher reaction temperature (423 K) and air pressure (30 bar) along with a much lower EtOH-to-Ru molar ratio of only 480 compared to 14 574 used in the present study.[9] All known heterogeneous Au-based catalysts, employed for the aerobic EtOH-to-AA oxidation, need a basic support material and much more drastic reaction conditions (*i.e.*, T > 453 K[5−7] or high oxygen pressure (30 bar)[8]) to reach comparable EtOH conversions.

Catalyst Stability. To test the stability of the Pt-based catalysts during the catalytic reactions, we carried out TEM, BET, and XPS analyses on catalysts, recovered from oxidation reactions, which lasted for 17 h. TEM micrographs and the corresponding histograms of the recovered catalysts are shown in Figure 6. As a result, the average particle sizes for $Pt^{L}@C^{K}$ and $(PtCu)^{L}@C^{K}$ were found to be 4.08 ± 0.65 nm (as-synthesized, 3.43 ± 0.43 nm) and 2.44 ± 0.43 (as-synthesized, 2.18 ± 0.23 nm), respectively, which indicated a higher stability of the bimetallic catalyst compared to the pure Pt-based one. TEM analysis conducted on recovered $(PtCu)^{L'}@C^{K}$ (d_m = 2.37 ± 0.38 nm, Figure S10) confirmed the high stability of the bimetallic NPs under real experimental conditions. We may thus infer from this latter result that the significantly lower catalytic activity found for $(PtCu)^{L'}@C^{K}$ compared to $(PtCu)^{L}@C^{K}$ in EtOH oxidation is not due to the change of the NP size during catalysis (*i.e.*, high thermal stability of the particles) but rather due to the partial burial of the NPs by the capping ligand. In this respect, a variable-temperature PXRD study carried out with $(PtCu)^{L}$ in an air atmosphere showed the loss of the capping ligand's crystallinity at 413 K (reaction temperature of catalytic reactions) due to the high mobility of the aliphatic chains, and on cooling, the

https://doi.org/10.1021/acs.inorgchem.2c04202
Inorg. Chem. XXXX, XXX, XXX−XXX

initial crystallinity of the capping ligand was not restored (Figure S11). In contrast, the PXRD pattern assigned to the PtCu alloy phase did change upon thermal treatment.

An XPS analysis of the recovered $(PtCu)^{L'}@C^{K}$ (Figure 7, trace b; Table S1) gave a surface metal atom-to-nitrogen atom

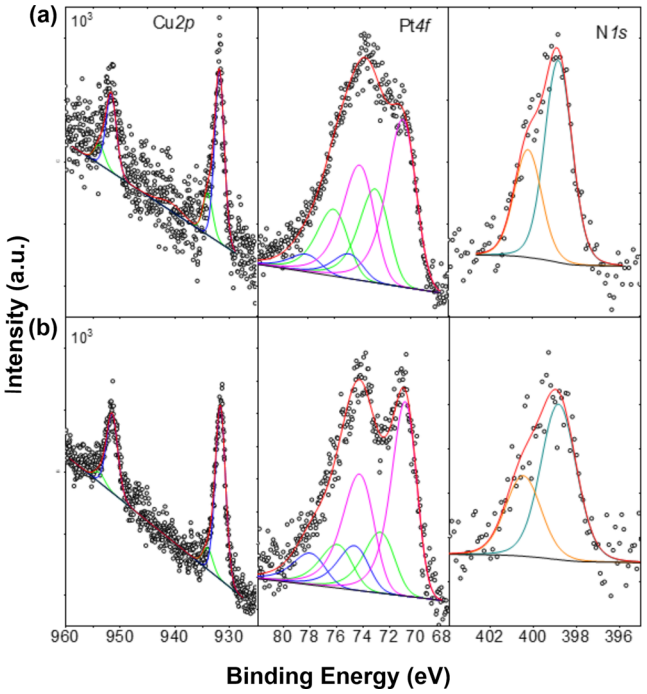

Figure 7. XPS spectra for $(PtCu)^{L'}@C^{K}$: as-synthesized (a) and recovered (b).

ratio of 0.3, which is identical to that of the as-synthesized catalysts (Figure 7, trace a). In addition, no N *1s* photoelectron peak assigned to the uncoordinated ligand (398.2 eV) has been detected. Both of these latter results confirmed that the bimetallic NPs are efficiently coordinated by the capping ligand. The Pt-to-Cu atom ratio decreased slightly from 0.7 to 0.6 (recovered catalyst), which is in line with the result obtained from the ICP-OES analysis carried out on the catalytic solution, showing a slightly higher Pt than Cu leaching (*i.e.*, Pt and Cu leaching of 5.0 and 3.7%, referred to the initial metal content). Interestingly, the ratio of the II/0 oxidation states of both metals changed during catalysis. The percentage of Pt(0) increased at the expense of the catalytically active Pt(II) sites (*i.e.*, 32.9 *vs* 22.8%, recovered catalyst), while the percentage of Cu(II) increased from 17.5 to 23.0%.

BET analysis conducted on recovered $Pt^{L}/(PtCu)^{L}@C^{K}$ (Figures S12 and S13) exhibited reduced surface areas of 11 and 13%, respectively, compared to the as-synthesized ones (Table S2), which might to some extent be due to the mobility of L on C^{K} at 413 K, which leads to a partial coverage of pores (*i.e.*, the cumulative pore volume decreased for both catalysts during catalysis) (Table S2).

A recycling experiment carried out with $(PtCu)^{L}@C^{K}$ showed a clear decrease of its catalytic performance (Table 2, entry 2 *vs* 1). We then activated the recovered catalysts (2nd run) with air (20 bar) for 5 h at 413 K and used them for a further catalytic reaction (Table 2, entry 3).

As a result, the EtOH conversion increased from 80.2 (2nd run) to 92.0% with a concomitant increase of the AA selectivity to 93.0% (Table 2, entry 3 *vs* 2). A further catalytic

Table 2. Recycling Experiments Conducted with $(PtCu)^{L}@C^{K}$[a]

entry	conv. (%)[b]	sel. AcA (%)[b]	sel. AA (%)[b]
1	97.5	2.0	98.0
2[c]	80.2	23.0	77.0
3[d]	92.0	7.0	93.0
4[e]	90.0	9.0	91.0

[a]Catalytic condition: $(PtCu)^{L}@C^{K}$ (Pt, 0.94 μmol), EtOH (13.7 mmol), water (50.0 mL), p(air) = 20 bar, T (413 K), t (40 h). [b]Defined as reported in Table 1. [c]2nd run. [d]3rd run after activation of the recovered catalyst (2nd run) with air (20 bar) at 413 K for 5 h. [e]4th run conducted as 3rd run.

reaction (Table 2, entry 4) proved that the catalytic performance of $(PtCu)^{L}@C^{K}$ was restored, provided that the recovered catalysts underwent an activation step with air (Table 2, entry 4 *vs* 3).

Electrochemical Oxidation of EtOH. $Pt^{L}/Cu^{L}/(PtCu)^{L}@C^{K}$ has been tested in the electrochemical oxidation of EtOH in an alkaline solution (*i.e.*, KOH, 1 M). To this purpose, we carried out cyclovoltammetry (CV) scans at room temperature and in the presence of a nitrogen atmosphere applying a scan rate of 50 mV/s in an interval of potential ranging from −1.2 to 0.4 V in the absence of EtOH (Figure 8A). The specific current (Sc) shown in Figure 8A/B has been referred to the amount of Pt present in both catalysts (*i.e.*, $Pt^{L}@C^{K}$, 1.6 $\mu g/cm^2$; and $(PtCu)^{L}@C^{K}$, 0.76 $\mu g/cm^2$).

A complete CV scan with $(PtCu)^{L}@C^{K}$ in the above-mentioned potential range showed two peaks: peak I, anodic scan at −0.7 V; and peak II, cathodic scan at −0.38 V. The former peak was assigned to the oxidation of surface Pt(0) to Pt(II)-OH species,[33,34] which were successively converted into PtO during the water oxidation reaction (WOR) (*i.e.*, onset 0.2 V) (Figure 8A). Peak II is associated with the reformation of active Pt(II)-OH species. In contrast, $Pt^{L}@C^{K}$ showed, under identical electrochemical conditions, only peak I as a very broad low-intense hump at −0.5 V (*i.e.*, potential shift of 0.2 V to a higher potential with respect to $(PtCu)^{L}@C^{K}$), confirming a much more favorable surface Pt(II)-(OH) species generation in the case of $(PtCu)^{L}@C^{K}$. CV scans conducted with the supported catalysts in the contemporary presence of KOH (1 M) and EtOH (0.2 M) in the same potential interval as reported above exhibited for $(PtCu)^{L}@C^{K}$ four distinct electrochemical steps in the course of a complete CV cycle, which have been assigned to the Pt(II)-OH formation (peak I), the EtOH oxidation (peak II), the reformation of the Pt(II)-OH (peak III), and the EtOH oxidation (peak IV) (Figure 8B). In the case of $Pt^{L}@C^{K}$, only peak II (Figure 8B) has been observed, showing a very low Sc (*i.e.*, maximum at −0.25 V), whereas $(PtCu)^{L}@C^{K}$ gave a Sc of 3.0 mA/μg(Pt) at −0.3 V (*i.e.*, *a* lower onset potential for EtOH oxidation compared to $Pt^{L}@C^{K}$ and hence a faster reaction kinetic in EtOH oxidation). This latter result, obtained with $(PtCu)^{L}@C^{K}$, is in complete accordance with the remarkable performances observed for related PtCu-nanoalloy-based electrocatalysts used for EtOH oxidation.[11] The Cu-alloying with Pt fulfills a dual role in the electrochemical oxidation of EtOH with $(PtCu)^{L}@C^{K}$: (*i*) copper alters the electronic structure of Pt, which brings about a weakening of the interaction between RCO_{ads} and Pt; and (*ii*) copper fosters the formation of surface hydroxide species on the surface in an alkaline solution. On the other hand, a pure Cu-based catalyst, such as $Cu^{L}@C^{K}$, gave

https://doi.org/10.1021/acs.inorgchem.2c04202
Inorg. Chem. XXXX, XXX, XXX−XXX

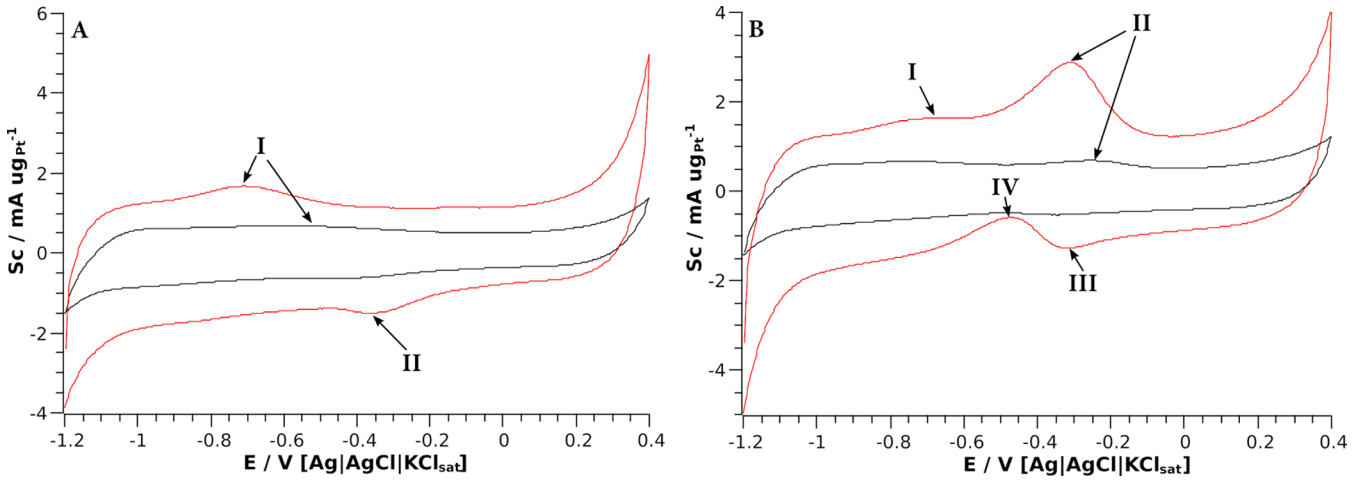

Figure 8. CV curves acquired for $Pt^{L}@C^{K}$ (black trace) and $(PtCu)^{L}@C^{K}$ (red trace) in KOH (1 M) (A) and in the presence of EtOH/KOH (1 M) (B).

no appreciable CV peak under identical electrochemical conditions, neither in the presence nor in the absence of EtOH (Figure S14).

Mechanistic Aspects of Aerobic EtOH Oxidation. From aerobic EtOH oxidation reactions (autoclave experiments) conducted in the absence and presence of $(PtCu)^{L}@C^{K}$, it was clearly seen that the first oxidation step (*i.e.*, conversion of EtOH to AcA) was the rate-determining step concerning the overall oxidation to AA (Scheme 2). This latter

Scheme 2. Proposed $(PtCu)^{L}$-Mediated Aerobic Oxidation of EtOH

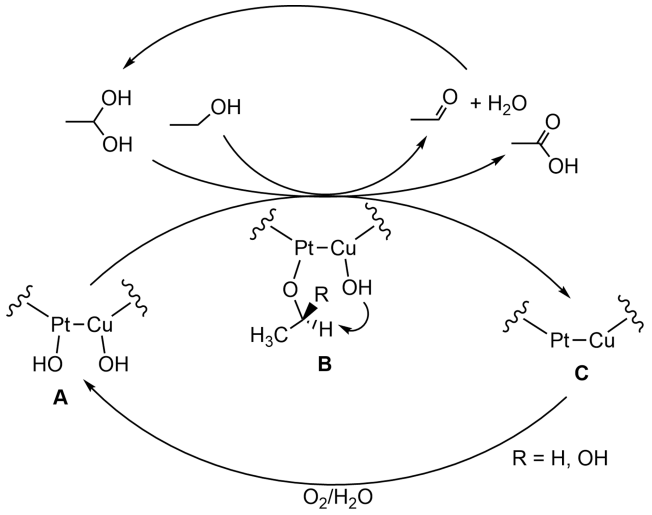

reaction is a Pt(II)-catalyzed dehydrogenation reaction, which comprised (i) the reaction of EtOH with the NP surface Pt(II)-OH species (A) to give the alcoholate intermediate B (i.e., activated form of the alcohol) (Scheme 2).[34] Cu notably increased the amount of surface Pt(II) due to its favorable electronic effect, which fosters oxidation of surface Pt(0).[35] (ii) An OH^{-}-mediated deprotonation of the α-hydrogen atom of the alcoholate yielding water and releasing AcA, which is in equilibrium with the corresponding hydrate as observed in the ^{1}H NMR spectra of the catalytic solutions (Figure S8); (iii) reduction of Pt(II) to Pt(0) upon release of AcA (intermediate C) (*i.e.*, XPS evidence of the recovered bimetallic catalyst). The reduction of the amount of catalytically active Pt(II) sites during aerobic alcohol oxidation is the real deactivation step of this bimetallic catalyst (*i.e.*, the catalytic activity can be restored by activating the recovered catalyst with air in the absence of a substrate).

The deprotonation of the alcoholate species is generally assumed to be the rate-determining step in the metal-catalyzed alcohol dehydrogenation reaction. Hence, the rate of the latter reaction step is strongly dependent on the concentration of surface OH^{-} anions.[36] In this context, NP surface Cu(II) sites along with the diamine functionalities of the capping ligand (*i.e.*, XPS evidence for hydrogen-bond interaction of NH functionalities of the capping ligand with surface M(II)-OH units) may be important OH^{-} shuttles since they are located in close proximity to the surface Pt(II)-alcoholate species.[36]

The catalytically active species A (Scheme 2) was then regenerated by the reaction of surface Pt(0) sites of species C with O_2 and water through an oxygen reduction reaction (ORR), where oxygen served as an electron scavenger (*i.e.*, oxygen has never been observed to be incorporated in the final oxidation product).[37] Hydrogen peroxide, which is the first oxygen reduction product of the ORR, is converted into OH^{-} anions, which compensate their consumption during alcoholate formation and the successive deprotonation step.[37]

The oxidation of AcA to AA is a much faster reaction compared to the dehydrogenation of EtOH at the same reaction temperature and even in the absence of a catalyst. The experimental fact, that along the NP-catalyzed AcA oxidation CO_2 was formed in amounts that were notably higher compared to the uncatalyzed reaction (Table 1), led to the conclusion that the oxidation of AcA to AA may follow the same reaction path as shown for EtOH using the acetaldehyde hydrate as the substrate (Scheme 2). The formation of CO_2, which implies a C−C bond scission, is an undesired reaction path, which is disfavored to some extent by the presence of surface Cu atoms (*i.e.*, CO_2 formation is lower with the bimetallic catalyst compared to the pure Pt- and Cu-based counterparts).

CONCLUSIONS

Diamine-stabilized PtCu NPs with a Pt:Cu (1:1) core and a Cu-enriched surface (Pt:Cu, 1:2) have been synthesized by the simultaneous reduction of a 1:1 mixture of Pt(II) and Cu(II)

https://doi.org/10.1021/acs.inorgchem.2c04202
Inorg. Chem. XXXX, XXX, XXX−XXX

bis-imine complexes with hydrogen. The diamine ligand, which bears C_{16}-alkyl chains, is strongly hydrophobic and interacts through the secondary amine functionalities with surface Pt(0) and M(II)-OH (M = Pt, Cu) sites. The heterogenization of the generated capped-bimetallic NPs brought about their successful usage as catalysts with an extremely low Pt loading of 0.34 wt % for the thermally conducted aerobic as well as electrochemical oxidation of EtOH to acetic acid. The presence of Cu in the alloy favored the formation of surface Pt(II)-OH species, which are key species (*i.e.*, promote the rate-determining dehydrogenation steps in alcohol oxidation reactions) in the aerobic as well as electrochemical oxidation of EtOH. As a consequence, in both types of catalytic processes, the bimetallic catalyst showed by far a higher catalytic activity compared to its pure Pt and Cu counterparts, which were synthesized following an analogous synthesis protocol. The presence of Cu in the alloy NPs notably reduces the formation of CO_2, which is high in the case of the pure Pt counterpart and which constitutes an undesired side product. The bimetallic catalyst, recovered from catalytic aerobic EtOH oxidation reactions, showed no alterations concerning the NP size and ligand coordination but showed a reduced amount of Pt(II) compared to the as-synthesized catalyst, which constitutes the real deactivation process. By an air activation step conducted in the absence of alcohol, the catalytic performance was restored to a large extent. The robustness of this bimetallic catalyst along with the very low amount of catalytically active Pt (0.34 wt %) and the presence of a diamine ligand, which might function as a hydroxide shuttle on the NP surface, made this catalyst unique for EtOH oxidation in water, outperforming, as far as the catalytic activity is concerned, the best NP-based Au[5−7] and Ru[8−11] catalysts, known for the aerobic EtOH oxidation.

EXPERIMENTAL SECTION

Materials. *N,N′*-Bis(hexadecyl)*α*-diimine was synthesized as reported previously.[4] EtOH, $PtCl_2$, $Cu(OAc)_2$, C_6H_6-d_6, $CHCl_3$-d, H_2O-d_2, and Nafion ion-exchange resin solution (5 wt %) were purchased from Aldrich and used without further purification. Dichloromethane was distilled over CaH_2, and *n*-pentane was stored over molecular sieves. Ketjenblack EC-600 JD (C^K, surface area of 1396 m^2/g) was purchased from Akzo Nobel.[31]

Syntheses of Pt^L, Cu^L, and $(PtCu)^L$. *N,N′*-Bis(hexadecyl)*α*-diimine[4] (400.0 mg, 0.79 mmol) reacted with $PtCl_2$ (211.0 mg, 0.79 mmol) or $Cu(OAc)_2$ (143.0 mg, 0.79 mmol) in deaereated CH_2Cl_2 (20 mL) at room temperature for 3 h. Afterward, the obtained solutions were separately transferred into teflonated autoclaves (70 mL) by suction. The autoclaves were successively pressurized with hydrogen (20 bar), heated to 333 K, and magnetically stirred for 12 h. Afterward, the autoclaves were cooled to room temperature, the excess gas was vented off, and the obtained suspension was concentrated to dryness. Then, the obtained solid was resuspended in *n*-pentane and filtered, and the *n*-pentane soluble fraction was concentrated to dryness by a vacuum pump at room temperature, obtaining the diamine (L)-capped NPs (Pt^L and Cu^L) as black and dark-red powder, respectively. Yield Pt^L: 450.0 mg; ICP-OES: Pt, 15.81 wt %. Yield Cu^L: 280.0 mg; ICP-OES: Cu, 1.88 wt %.

A solution containing *N,N′*-bis(hexadecyl)*α*-diimine (400.0 mg, 0.79 mmol) and $Cu(OAc)_2$ (143.0 mg, 0.79 mmol) in deaereated CH_2Cl_2 (20 mL) was added to a deaereated CH_2Cl_2 solution of *N,N′*-bis(hexadecyl)*α*-diimine (400.0 mg, 0.79 mmol) and $PtCl_2$ (211.0 mg, 0.79 mmol) at room temperature. The combined solution was then transferred under a nitrogen atmosphere into a teflonated autoclave by suction. The autoclave was then successively pressurized with hydrogen (20 bar), heated to 333 K, and mechanically stirred for 12 h. Afterward, the workup procedure was identical to that described above for the synthesis of Pt^L and Cu^L, yielding $(PtCu)^L$ as a black solid. Yield $(PtCu)^L$: 560.0 mg; ICP-OES: Pt, 13.94 wt %; Cu, 4.86 wt %.

Syntheses of $Pt^L/(PtCu)^L/(PtCu)^{L'}/Cu^L@C^K$. Pt^L (100.0 mg) and $(PtCu)^L$ (50.0 mg) were separately dissolved in *n*-pentane (10 mL) and added to sonicated suspensions of C^K in the same solvent using 2.0 and 1.8 g of C^K for Pt^L and $(PtCu)^L$, respectively. Since Cu^L showed a low Cu content (1.88 wt %), 43.0 mg of Cu^L was dissolved in *n*-pentane (10 mL) and added to a sonicated suspension of C^K (57.0 mg). The C^K suspensions were magnetically stirred at room temperature under a nitrogen atmosphere for 1 h, followed by evaporation of the solvent to dryness. The obtained black solids were analyzed by ICP-OES: $Pt^L@C^K$: Pt, 0.75 wt %; $(PtCu)^L@C^K$: Pt, 0.38 wt %; Cu, 0.13 wt %; $Cu^L@C^K$: Cu, 0.79 wt %. $(PtCu)^{L'}@C^K$ was synthesized as $(PtCu)^L@C^K$ using a higher loading of $(PtCu)^L$: ICP-OES: Pt, 2.04 wt %; Cu, 0.81 wt %.

Catalyst Characterization. Powder X-ray diffraction (PXRD) spectra were acquired at room temperature with a PANalytical X'PERT PRO powder diffractometer, using Cu K*α* radiation (λ = 1.5418 Å) and a Si zero background wafer as the sample holder. The spectra were acquired at room temperature in the 2Θ range of 5.0−80.0° using a step size of 0.1050°. Variable-temperature PXRD spectra were acquired by means of an HTK 1500 heating chamber.

Transition electron microscopic (TEM) measurements were carried out on a TEM PHILIPS CM 12 instrument, equipped with an OLYMPUS Megaview G2 camera, and using an accelerating voltage of 100 keV. Samples, suitable for the analyses, were prepared by dropping a water suspension of the carbon-supported catalysts on a holey film of a 300-mesh Cu grid, followed by evaporation of the solvent at room temperature. The average particle size, characterized by the mean particle diameter (d_m), was calculated by applying the following equation: $d_m = \sum d_i n_i / \sum n_i$, where n_i corresponds to the number of particles of diameter d_i.

X-ray photoelectron spectroscopic (XPS) analyses were carried out in a UHV chamber (10^{-9} mbar) equipped with nonmonochromatized Al radiation ($h\nu$ = 1486.6 eV) and a hemispherical electron energy analyzer. The operating power of the X-ray source was 150 W, and photoelectrons were collected normal to the sample surface, maintaining the angle between the analyzer axis and the X-ray source fixed at 54.5°. All samples were adsorbed on carbon tape, and XPS spectra were acquired in a fixed analyzer transmission mode with a pass energy of 44.0 eV. The spectra were analyzed using CasaXPS software, and linear or Shirley functions have been used to subtract the background. The deconvolution of XPS spectra has been performed by applying a combination of Gaussian and Lorentzian functions (70/30 ratio), and binding energies (B.E.) were calibrated upon fixing the C1s component of the carbon tape at 285.1 eV.[26]

The Brunauer−Emmett−Teller (BET) specific surface area of C^K-supported catalysts was determined by nitrogen adsorption at 77 K using a Micromeritics ASAP 2020 analyzer. The samples were pretreated at 393 K under vacuum (3.95×10^{-5} bar) for 15 h. The BET surface area was calculated in the pressure range between 0.1 and 0.22 p/p°, while the pore size was calculated by means of the BJH method (17.00−3000.00 Å range).

^{1}H NMR spectra were acquired at room temperature using a Bruker Avance 400 MHz spectrometer and $CHCl_3$-d, C_6H_6-d_6, or H_2O-d_2 as a solvent. For catalytic solutions, an Evans tube charged with D_2O was used.

ICP-OES were carried out with an ICP-optical emission dual-view Perkin Elmer OPTIMA 8000 apparatus.

Cyclovoltammetry (CV) Measurements. CV experiments were performed in a classical three-electrode cell with a glassy carbon working electrode on which was supported the carbon-containing catalyst by drop casting and successive drying. A platinum wire was used as the counter electrode and $(Ag/AgCl/KCl_{sat})$ as the reference electrode. Hence, if not otherwise stated, all potentials reported have been referenced to saturated Ag/AgCl. All CV experiments were conducted with deaereated solutions (*i.e.*, nitrogen gas was bubbled through the solution prior to the experiment, and the headspace of the

https://doi.org/10.1021/acs.inorgchem.2c04202
Inorg. Chem. XXXX, XXX, XXX−XXX

solutions was kept under a nitrogen atmosphere during the experiment).

The glassy carbon electrode containing the supported catalysts was prepared as follows. The carbon-supported catalysts (*i.e.*, $Pt^L/PtCu^L/Cu^L@C^K$) (20.0 mg) were dispersed in a solvent mixture containing distilled water (0.5 mL) and *iso*-propanol (1.5 mL). The obtained dispersions were sonicated at room temperature for 30 min; then, a portion of each dispersion was drop-cast onto a glassy carbon electrode (*i.e.*, surface area of 0.196 cm^2), which had been polished with alumina prior to use. After drying the glassy carbon electrode by means of a nitrogen flow, a Nafion solution binder dissolved in *iso*-propanol (2.6 μL, 0.5 wt %) was drop-cast on the deposited catalyst and dried at room temperature. Comparative CV measurements (*i.e.*, scan rate of 50 mV/s) were conducted in water solutions containing KOH (1 M) and KOH (1 M)/EtOH (5 vol%).

Catalytic Reactions. A teflonated autoclave (320 mL) was successively charged with EtOH (13.7 or 54.8 mmol), water (50 mL), and the desired amount of catalyst ($Pt^L/(PtCu)^L/Cu^L@C^K$). The autoclave was then sealed, pressurized with air, heated to 413 K, and mechanically stirred (900 rpm). Once the latter reaction temperature was reached, the air pressure was adjusted to 20 bar and stirring was continued for the desired reaction time. Afterward, the autoclave was cooled by means of an ice water bath to 283 K and a fraction of the autoclave's headspace gas withdrawn and analyzed by GC-TCD. Then, the excess of gas was vented off, the suspension centrifuged, and the solution decanted. The obtained solid was washed twice with water (2 × 10 mL) before drying in a vacuum oven at 323 K. The dried solid catalyst was then used for recycling experiments, following the above-reported procedure.

The catalytic solutions were analyzed by HPLC (*i.e.*, Shimadzu apparatus equipped with an Aminex HPX-87H chromatographic column (300 mm × 7.8 mm, BIO RAD) and an RID 10A detector) using sulfuric acid (0.005 M) with a flow rate of 0.4 mL/min and a column temperature of 308 K. The quantification of the residual EtOH and of the organic products formed during catalysis was based on calibration curves made for each compound, while ^1H NMR spectra were acquired by means of an Evans tube charged with D_2O. The headspace of the autoclave was analyzed by means of a Shimadzu 2010 apparatus, using He as the carrier gas, a TCD-17 detector, and a Carboxen (Supelco) 1010 PLOT fused silica capillary column (30 m × 0.32 mm).

The recycled catalyst was reactivated in an autoclave at 413 K with an air pressure of 20 bar for 5 h.

■ ASSOCIATED CONTENT

Supporting Information

The Supporting Information is available free of charge at https://pubs.acs.org/doi/10.1021/acs.inorgchem.2c04202.

PXRD spectra for Cu^L (room temperature) and for $(PtCu)^L$ (variable temperature); TEM images for Cu^L and $(PtCu)^{L'}@C^K$; table of XPS data for the catalysts; BET analyses for the supported catalysts; HPLC and ^1H NMR spectra for selected catalytic solutions; variable-temperature PXRD spectra for $(PtCu)^L@C^K$; and CV traces for Cu^L (PDF)

■ AUTHOR INFORMATION

Corresponding Author

Werner Oberhauser − *Istituto di Chimica dei Composti Organometallici (CNR-ICCOM), 50019 Sesto Fiorentino, Italy*; orcid.org/0000-0002-9800-1700; Email: werner.oberhauser@iccom.cnr.it

Authors

Lorenzo Poggini − *Istituto di Chimica dei Composti Organometallici (CNR-ICCOM), 50019 Sesto Fiorentino, Italy*

Laura Capozzoli − *Istituto di Chimica dei Composti Organometallici (CNR-ICCOM), 50019 Sesto Fiorentino, Italy*

Marco Bellini − *Istituto di Chimica dei Composti Organometallici (CNR-ICCOM), 50019 Sesto Fiorentino, Italy*; orcid.org/0000-0001-6901-7781

Jonathan Filippi − *Istituto di Chimica dei Composti Organometallici (CNR-ICCOM), 50019 Sesto Fiorentino, Italy*

Francesco Vizza − *Istituto di Chimica dei Composti Organometallici (CNR-ICCOM), 50019 Sesto Fiorentino, Italy*; orcid.org/0000-0003-3850-0249

Complete contact information is available at: https://pubs.acs.org/10.1021/acs.inorgchem.2c04202

Author Contributions

The manuscript was written jointly by all authors concerned, and they have given approval to the final version of the manuscript.

Notes

The authors declare no competing financial interest.

■ ACKNOWLEDGMENTS

The authors thank the Italian National Research Council (CNR) for having access to the microscopy facility "Ce.M.E.−Centro Microscopie Elettroniche Laura Bonzi" and "Ente Cassa di Risparmio di Firenze" (Grant Number n.2013.0878) and Regione Toscana POR FESR 2014-2020, FELIX (Fotonica ed Elettronica Integrate per l'Industria, Grant Number 6455) for financial support of Ce.M.E. Thanks are also due to Carlo Bartoli for his assistance in the maintenance of the high-pressure equipment and to B. Cortigiani for his assistance in using the CeTeCS platform. The authors also acknowledge the Progetto Dipartimenti di Ecellenza 2018-2022 (ref no. B96C1700020008) and the "Accordo di Programma MiTE-ENEA PNRR Investimento 3.5 Ricerca Sviluppo sull' Idrogeno, LA 1.1.24" for financial support.

■ REFERENCES

(1) Deshmukh, G.; H Manyar, H. Biotechnological Applications of Biomass. In *Production Pathways of Acetic Acid and Its Versatile Applications in the Food Industry*, Basso, T. S.; Basso, T. O.; Basso, L. C., Eds.; IntechOpen, 2021, Chapter 15.

(2) Kalck, P.; Le Berre, C.; Serp, P. Recent Advances in the Methanol Carbonylation Reaction into Acetic Acid. *Coord. Chem. Rev.* **2020**, *402*, No. 213078.

(3) Sano, K.-i.; Uchida, H.; Wakabayashi, S. A New Process for Acetic Acid Production by Direct Oxidation of Ethylene. *Catal. Survey Japan* **1999**, *3*, 55−60.

(4) Oberhauser, W.; Evangelisti, C.; Capozzoli, L.; Manca, G.; Casaletto, M. P.; Vizza, F. Selectivity Switch in the Aerobic 1,2-Propandiol Oxidation Catalyzed by Diamine-Stabilized Palladium Nanoparticles. *ChemCatChem* **2021**, *13*, 2896−2906.

(5) Christensen, C. H.; Jørgensen, B.; Rass-Hansen, J.; Egeblad, K.; Madsen, R.; Klitgaard, S. K.; Hansen, S. M.; Hansen, M. R.; Andersen, H. C.; Riisager, A. Formation of Acetic Acid by Aqueous-Phase Oxidation of Ethanol with Air in the Presence of a Heterogeneous Gold Catalyst. *Angew. Chem., Int. Ed.* **2006**, *45*, 4648−4651.

(6) Jorgensen, B.; Christiansen, S. E.; Dahl Thomsen, M. L.; Christensen, C. H. Aerobic Oxidation of Aqueous Ethanol Using Heterogeneous Gold Catalysts: Efficient Routes to Acetic Acid and Ethyl Acetate. *J. Catal.* **2007**, *251*, 332−337.

(7) Mostrou, S.; Newton, A.; Tarcevski, A.; Nagl, A.; Föttinger, K.; van Bokhoven, J. Titanium-Anchored Gold on Silica for Enhanced

Catalytic Activity in Aqueous Ethanol Oxidation. *Ind. Eng. Chem. Res.* **2021**, *60*, 1564−1575.
(8) Hu, W.; Li, D.; Yang, Y.; Li, T.; Chen, H.; Liu, P. Copper Ferrite Supported Gold Nanoparticles as Efficient and Recyclable Catalyst for Liquid-Phase Ethanol Oxidation. *J. Catal.* **2018**, *357*, 108−117.
(9) Ding, H.; Qi, X.; Yun, X.; Ge, J.; Tian, Y.; Lei, X.; Zhang, F. Confined Ruthenium Nanoparticles as an Efficient Catalyst for Aerobic Oxidation of Aqueous Ethanol to Acetic Acid. *ACS Sustainable Chem. Eng.* **2022**, *10*, 9687−9696.
(10) Gorbanev, Y. Y.; Kegnaes, S.; Hanning, C. W.; Hansen, T. W.; Riisager, A. Acetic Acid Formation by Selective Aerobic Oxidation of Aqueous Ethanol over Heterogeneous Ruthenium Catalysts. *ACS Catal.* **2012**, *2*, 604−612.
(11) Huang, X.-Y.; Wang, A.-J.; Zhang, X.-F.; Zhang, L.; Feng, J.-J. One −Step Synthesis of PtCu Alloyed Nanocages with Highly Open Structures as Bifunctional Electrocatalysts for Oxygen Reduction and Polyhydric Alcohol Oxidation. *ACS Appl. Energy Mater.* **2018**, *1*, 5779−5786.
(12) Li, T.; Jing, T.; Jia, X.; Guo, S.; Li, W.; Yue, H.; Luo, Z. Galvanic Replacement Mediated 3D Porous PtCu Nano-Frames for Enhanced Ethylene Glycol Oxidation. *Chem. Commun.* **2019**, *55*, 14526−14529.
(13) Huang, L.; Zhang, W.; Li, P.; Song, Y.; Sheng, H.; Du, Y.; Wang, Y.-G.; Wu, Y.; Hong, X.; Ding, Y.; Yuan, X.; Zhu, M. Exposing Cu-rich {110} Active Facets in PtCu Nanostars for Boosting Electrochemical Performance Toward Multiple Liquid Fuels Electrooxidation. *Nano Res.* **2019**, *12*, 1147−1153.
(14) Liu, T.; Wang, K.; Yuan, Q.; Shen, Z.; Wang, Y.; Zhang, Q.; Wang, X. Monodispersed Sub-5.0 nm PtCu Nanoalloys as Enhanced Bifunctional Electrocatalysts for Oxygen Reduction Reaction and Ethanol Oxidation Reaction. *Nanoscale* **2017**, *9*, 2963−2968.
(15) Li, D.; Cai, K.; Wu, L.; Zuo, Y.; Yin, W.; Zhang, H.; Lu, Z.; Zhu, G.; Han, H. Ammonia Mediated One-Step Synthesis of Three-Dimensional Porous Pt_xCu_{100-x} Nanochain Networks with Enhanced Electrocatalytic Activity toward Polyhydric Alcohol Oxidation. *ACS Sustainable Chem. Eng.* **2017**, *5*, 11086−11095.
(16) Chen, Y.-Z.; Gu, B.; Uchida, T.; Liu, J.; Liu, X.; Ye, B.-J.; Xu, Q.; Jiang, H.-L. Location Determination of Metal Nanoparticles Relative to a Metal-Organic Framework. *Nat. Commun.* **2019**, *10*, No. 3462.
(17) Shiraishi, Y.; Sakamoto, H.; Sugano, Y.; Ichikawa, S.; Hirai, T. Pt-Cu Bimetallic Alloy Nanoparticles Supported on Anatase TiO_2: Highly Active Catalysts for the Aerobic Oxidation Driven by Visible Light. *ACS Nano* **2013**, *7*, 9287−9297.
(18) Zhou, S.; Varughese, B.; Eichhorn, B.; Jackson, G.; McIlwrath, K. Pt-Cu Core-Shell and Alloy Nanoparticles for Heterogeneous NO_x Reduction: Anomalous Stability and Reactivity of a Core-Shell Nanostructure. *Angew. Chem., Int. Ed.* **2005**, *44*, 4539−4543.
(19) Zhang, X.; Cui, G.; Feng, H.; Chen, L.; Wang, H.; Wang, B.; Zhang, X.; Zheng, L.; Hong, S.; Wei, M. Platinum-Copper Single Atom Alloy Catalysts with High Performance Towards Glycerol Hydrogenolysis. *Nat. Commun.* **2019**, *10*, No. 5812.
(20) Ferrando, R.; Jellinek, J.; Johnston, R. L. Nanoalloys: From Theory to Applications of Alloy Clusters and Nanoparticles. *Chem. Rev.* **2008**, *108*, 845−910.
(21) Sankar, M.; Dimitratos, N.; Miedziak, P. J.; Wells, P. P.; Kiely, C. J.; Hutchings, G. J. Designing Bimetallic Catalysts for a Green and Sustainable Future. *Chem. Soc. Rev.* **2012**, *41*, 8099−8139.
(22) Rubinov, E.; Diab, M.; Volokh, M.; Mokari, T. Insight Into the Formation Mechanism of PtCu Alloy Nanoparticles. *CrystEngComm.* **2014**, *16*, 9493−9500.
(23) Yan, W.; Zhang, D.; Zhang, Q.; Sun, Y.; Zhang, S.; Du, F.; Jin, X. Synthesis of PtCu-Based Nanocatalysts: Fundamentals and Emerging Challenges in Energy Conversion. *J. Energy Chem.* **2022**, *64*, 583−606.
(24) Polte, J. Fundamental Growth Principles of Colloidal Metal Nanoparticles -A New Perspective. *CrystEngComm* **2015**, *17*, 6809−6830.
(25) Qazi, S. J. S.; Rennie, A. R.; Cockcroft, J. K.; Vickers, M. Use of Wide-Angle X-Ray Diffraction to Measure Shape and Size of Dispersed Colloidal Particles. *J. Colloid Interface Sci.* **2009**, *338*, 105−110.
(26) Ono, L. K.; Yuan, B.; Heinrich, H.; Cuenya, B. R. Formation and Thermal Stability of Platinum Oxides on Size-Selected Platinum Nanoparticles: Support Effects. *J. Phys. Chem. C* **2010**, *114*, 22119−22133.
(27) Kang, W.; Li, R.; Wei, D.; Xu, S.; Wei, S.; Li, H. CTAB-Reduced Synthesis of Urchin-Like Pt-Cu Alloy Nanostructures and Catalysis Study Towards the Methanol Oxidation Reaction. *RSC Adv.* **2015**, *5*, 94210−94215.
(28) da Silva, F. P.; Fiorio, J. L.; Gonçalves, R. V.; Teixeira-Neto, E.; Rossi, L. M. Synergic Effect of Copper and Palladium for Selective Hydrogenation of Alkynes. *Ind. Eng. Chem. Res.* **2018**, *57*, 16209−16216.
(29) Kerber, S. J.; Bruckner, J. J.; Wozniak, K.; Seal, S.; Hardcastle, S.; Barr, T. L. The Nature of Hydrogen in X-Ray Photoelectron Spectroscopy: General Patterns from Hydroxides to Hydrogen Bonding. *J. Vac. Sci. Technol. A* **1996**, *14*, 1314−1320.
(30) Ballerini, G.; Ogle, K.; Barthés-Labrousse, M.-G. The Acid-Base Properties of the Surface of Native Zinc Oxide Layers: An XPS Study of Adsorption of 1,2-Diaminoethane. *Appl. Surf. Sci.* **2007**, *253*, 6860−6867.
(31) Bevilacqua, M.; Bianchini, C.; Marchionni, A.; Filippi, J.; Lavacchi, A.; Miller, A. M.; Oberhauser, W.; Vizza, F.; Granozzi, G.; Artiglia, L.; Annen, S. P.; Krumeich, F.; Grützmacher, H. Improvement in the Efficiency of an OrganoMetallic Fuel Cell by Turning the Molecular Architecture of the Anode Elctrocatalyst and the Nature of the Carbon Support. *Energy Environ. Sci.* **2012**, *5*, 8608−8620.
(32) Mostrou, S.; Nagl, A.; Ranocchiari, M.; Föttinger, K.; van Bokhoven, J. The Catalytic and Radical Mechanism for Ethanol Oxidation to Acetic Acid. *Chem. Commun.* **2019**, *55*, 11833−11836.
(33) Liang, Z. X.; Zhao, T. S.; Xu, J. B.; Zhu, L. D. Mechanism Study of the Ethanol Oxidation Reaction on Palladium in Alkaline Media. *Electrochim. Acta* **2009**, *54*, 2203−2208.
(34) Tripković, A.; Popović, K. Dj.; Lović, J. D. The Influence of the Oxygen-Containing Species on the Electrooxidation of the C_1-C_4 Alcohols at some Platinum Single Crystal Surfaces in Alkaline Solution. *Electrochim. Acta* **2001**, *46*, 3163−3173.
(35) Najafishirtari, S.; Ortega, K. F.; Douthwaite, M.; Pattisson, S.; Hutchings, G. J.; Bondue, C. J.; Tschulik, K.; Waffel, D.; Peng, B.; Deitermann, M.; Busser, G. W.; Muhler, M.; Behrens, M. A. Perspective on Heterogeneous Catalysts for the Selective Oxidation of Alcohols. *Chem Eur. J.* **2021**, *27*, 16809−16833.
(36) Douthwaite, M.; Powell, N.; Taylor, A.; Ford, G.; López, J. M.; Solsona, B.; Yang, N.; Sanahuja-Parejo, O.; He, Q.; Morgan, D. J.; Garcia, T.; Taylor, S. H. Glycerol Selective Oxidation to Lactic over AuPt Nanoparticles; Enhancing Reaction Selectivity and Understanding by Support Modification. *ChemCatChem* **2020**, *12*, 3097−3107.
(37) Zope, B. N.; Hibbitts, D. D.; Neurock, M.; Davis, R. J. Reactivity of the Gold/Water Interface During Selective Oxidation Catalysis. *Science* **2010**, *330*, 74−78.

https://doi.org/10.1021/acs.inorgchem.2c04202
Inorg. Chem. XXXX, XXX, XXX−XXX